Geopersia 2026, 16(1): 195-209
DOI: 10.22059/geope.2025.399987.648833

RESEARCH PAPER

2.5D Inversion of Airborne Time Domain Electromagnetic Data through Constrained Occam and Conjugate Gradient Method to Image a Polymetallic Deposit

Ali Jafarabadi, Maysam Abedi *, Ali Moradzadeh

School of Mining Engineering, College of Engineering, University of Tehran, Tehran, Iran

Received: 03 August 2025, Revised: 08 October 2025, Accepted: 27 October 2025

Abstract

Porphyry deposits are major sources of copper, molybdenum, and gold. Airborne time-domain electromagnetic (TDEM) surveys play a crucial role in identifying conductive sulfide mineralization, particularly in geologically complex environments. This study employs 2.5D inversion of airborne TDEM data to image the Bell polymetallic deposit in British Columbia, Canada, offering improved accuracy over 1D methods in resolving complex geological structures, while maintaining lower computational demands than full 3D modeling. The methodology employs constrained Occam inversion with conjugate gradient optimization implemented in the ArjunGUI software. Forward modeling was conducted using finite-element methods in the wavenumber domain to simulate subsurface conductivity, and the results were subsequently transformed into time-domain using Fourier techniques.The inversion minimizes data misfit and model roughness using Lagrange multipliers and parameter bounds. Geological constraints, such as fixed background resistivities, were incorporated to ensure model accuracy. Inversion of an airborne TDEM survey line across the Bell deposit produced a resistivity model that highlights significant low-resistivity anomalies at approximately 100 m depth. These anomalies are associated with phyllic alteration zones and inferred fault structures that facilitated fluid circulation. High-resistivity areas delineate potassic alteration zones, which align with prior geophysical data and confirm the model's reliability. The 2.5D inversion provided enhanced accuracy compared to 1D methods and greater efficiency than 3D modeling, thereby facilitating targeted exploration in porphyry systems. The main limitations include high noise in late-time channels and potential mesh distortions due to topography. These limitations suggest that improvements in mesh discretization are needed for for future applications. Overall, this technique demonstrates the potential of 2.5D TDEM inversion as a practical and efficient approach for subsurface imaging and resource evaluation in polymetallic deposits.

Keywords: Airborne TDEM, 2.5D Inversion, Constrained Occam, Polymetallic Deposit, Porphyry Alteration.

Introduction

Porphyry deposits, often polymetallic in nature with significant copper and gold potential alongside molybdenum and other metals, constitute the world's foremost sources of copper and molybdenum, as well as major sources of gold (Sinclair, 2007). Airborne time-domain electromagnetic (TDEM) methods have emerged as a cornerstone in mineral exploration, particularly for detecting conductive sulfide mineralization in such deposits. They offer rapid coverage due to their ability to cover vast areas rapidly and provide deep penetration while maintaining sensitivity to conductivity contrasts (Palacky & West, 1991; Smith, 2014). These

* Corresponding author e-mail: maysamabedi@ut.ac.ir

techniques exploit transient electromagnetic pulses to measure subsurface responses, enabling the identification of polymetallic ore bodies in challenging terrains, where traditional ground methods are impractical (Palacky & West, 1991). Recent advancements have enhanced their resolution for both shallow and deep targets, making them indispensable for mapping complex geological structures associated with economic mineralization (Auken et al., 2017; Smith, 2014). The TDEM method is particularly well-suited for porphyry deposits, which typically exhibit large-scale alteration zones and conductive sulfide mineralization (e.g., chalcopyrite and pyrite) that generate pronounced conductivity contrasts readily detectable by TDEM (Guo et al., 2020; Palacky & West, 1991). This approach enhances the resolution of complex subsurface structures, making it effective for delineating fault-controlled mineralization and alteration patterns characteristic of porphyry systems (Wilson et al., 2006). Furthermore, the method also proves effective for other polymetallic deposits, such as volcanogenic massive sulfide (VMS) and skarn systems, which similarly feature high-conductivity sulfides due to resistivity differences from their host rocks (Guo et al., 2020; McMillan et al., 2014; Núñez et al., 2023). However, successful implementation in these deposit types may necessitate adjustments in survey design or inversion parameters to address variations in geometry and host rock properties (McMillan et al., 2014; Núñez et al., 2023). Consequently, the flexibility of the TDEM method supports its broader utility in diverse mineral exploration contexts, particularly where resistivity contrasts enable clear differentiation of economic mineralization.

Compared to magnetometry and electrical resistivity tomography (ERT) methods, the main advantage of the TDEM method lies in its direct sensitivity to electrical conductivity contrasts, enabling superior detection and imaging of concealed sulfide mineralization in polymetallic deposits with greater depth penetration (Oldenburg et al., 1997; Shah et al., 2013). Magnetometry primarily identifies magnetic property variations, such as magnetite destruction in alteration zones, but may overlook non-magnetic sulfides, while ERT detects electrical resistivity and chargeability anomalies associated with disseminated mineralization yet often produces widespread responses not unique to economic deposits (Oldenburg et al., 1997; Shah et al., 2013). Therefore, airborne TDEM offers enhanced resolution and efficiency for complex geological settings.

In complex geological environments, where other features obscure the target signal, direct interpretation is challenging (Oldenburg & Pratt, 2007). Surveys aim to identify exploration targets, map large-scale geology for potential deposit areas.Modeled images can then reveal mineralization or associated structures, offering insights beyond simple data maps (Oldenburg, 1999; Oldenburg & Pratt, 2007). Progress in computing and optimization techniques has led to algorithms that model geophysical data to build subsurface property images (Oldenburg, 1999). In this context, these methods recover distributions of physical properties to explain the observations, often through 1D/2D/3D models tailored to exploration demands (Oldenburg & Pratt, 2007).

Although 1D inversion remains common for airborne electromagnetic data due to the difficulties in constructing 2D/3D models that handle survey complexities (Li et al., 2016), it frequently struggles to image basic 2D/3D targets, especially under intricate geological settings (Chang-Chun et al., 2015; Ellis, 1998; Raiche et al., 2001; Wilson et al., 2006). For instance, when topography is pronounced or subsurface features show 2D or 3D forms, 1D approaches yield unreliable results for geological structures (Chang-Chun et al., 2015). In contrast, 3D modeling poses significant computational hurdles, as it requires solving as many large linear systems of equations as there are transmitter positions in the survey (Wilson et al., 2006). 2D inversions, however, offer improved accuracy in resolving conductive features over 1D methods while demanding fewer resources and simpler parallel processing than 3D ones (Yu & Haber, 2012). Often, airborne 2D inversion acts as a 2.5D problem, given that geological strikes extend laterallyin two dimensions but the transmitter loop is 3D (Chang-Chun et al., 2015).

Building on these benefits, various algorithms for 2.5D modeling of time-domain electromagnetic data have been developed. Everett and Edwards (1993), Sugeng et al. (1993), and Unsworth et al. (1993) developed electromagnetic algorithms based on the standard 2.5D version of Maxwell's equations in the early 1990s (Everett & Edwards, 1993; Sugeng et al., 1993; Unsworth et al., 1993). These algorithms have been applied to various airborne electromagnetic problems (e.g., (Abubakar et al., 2008; Raiche et al., 2003; Wilson et al., 2006)). Subsequent developments have further advanced 2.5D modeling and inversion techniques for airborne TDEM applications (Engebretsen et al., 2022; Ke et al., 2023; Paterson et al., 2016; Silic et al.). One practical outcome of these efforts is ArjunGUI © University of Oulu, a free software for 2.5D inversion of airborne TDEM data, built on ArjunAir developed by Wilson et al. (2006) for CSIRO/Amira consortia (Wilson et al., 2006). It computes frequency-domain responses using finite elements and applies Fourier transform to obtain time-domain results. For inversion, ArjunGUI employs constrained Occam with conjugate gradient (Occam+CG), which minimizes both data misfit and model roughness via Lagrange multipliers for smooth resistivity distributions, while CG efficiently solves large equations to reduce computation time (Pirttijärvi, 2014).

In this study, we employ the 2.5D inversion of airborne TDEM data via the constrained Occam and conjugate gradient approach to delineate the Bell polymetallic deposit, situated on the Newman Peninsula at the northern tip of Babine Lake. Utilizing the resistivity model derived from a single profile inversion, we construct a geological framework that emphasizes alteration zones for improved interpretation of the deposit's subsurface architecture, geological features, and mineralization potential.

Methodology

The inversion of time-domain electromagnetic (TDEM) data is inherently non-unique, as multiple models can fit the observations. Traditional regularization alone may not yield the most reliable solution, particularly in complex polymetallic settings. Incorporating prior geological information through constraints enhances accuracy by guiding model parameters toward realistic structures. To address this, the study employs constrained Occam inversion with conjugate gradient optimization. Forward modeling provides predicted responses for subsurface conductivities, while inversion iteratively updates the model by evaluating misfit and sensitivities derived from these forward computations, as detailed below.

TDEM Forward Modeling

The forward modeling of the time-domain electromagnetic (TDEM) response follows the approach in Sugeng et al. (1993) (Sugeng et al., 1993). The process begins by representing the subsurface conductivity as a two-dimensional function, $\sigma(x,z)$, which varies laterally and with depth while remaining constant along the strike direction (y). The total field can be expressed as the sum of a primary reference field and a secondary field, with the primary field calculated for a uniform half-space of conductivity $\sigma_N(z)$. This decomposition, $\sigma(x,z)=\sigma_N(z)+\sigma_R(x,z)$, reduces computational complexity by allowing the reference field to be computed analytically, while the secondary field accounts for lateral variations in conductivity.

The governing equations for the secondary electric and magnetic fields are derived from Maxwell's equations, with the distributed source term J_D expressed as:

$$J_D(x,y,z)=\sigma_R(x,z)E_n(x,y,z) \quad (1)$$

These relations lead to six coupled field equations that, under the assumption of strike invariance, are reduced to two equations in the k_y wavenumber domain for the along-strike field components, $\tilde{E}_{sy}$ *and* $\tilde{H}_{sy}$. The transformation into the k_y domain is given by:

$$F(x,y,z)=\left(\frac{1}{\pi}\right)\int_0^{\infty}\hat{F}(x,k_y,z)\cos(k_y y)dy \tag{2}$$

This formulation simplifies the solution process by ensuring continuity of $\tilde{E}_{sy}$ *and* $\tilde{H}_{sy}$ across conductivity interfaces, which facilitates computation using finite-element methods, as described below.

After deriving the coupled equations for $\tilde{E}_{sy}$ *and* $\tilde{H}_{sy}$ in the k_y domain, the solution proceeds using an isoparametric finite-element formulation. This approach enables the computational mesh to adapt to complex subsurface geometries, including regions with curved or inclined conductivity boundaries, while maintaining accuracy with fewer elements compared to conventional linear finite-element or finite-difference schemes.

Within each finite element, the electric and magnetic field components are approximated by a polynomial basis of the form:

$$a_0+a_1x+a_2x^2+a_3z+a_4z^2+a_5xz+a_6xz^2+a_7x^2z$$

allowing smooth interpolation across irregular element shapes. The field solutions in the j th element are represented by eight isoparametric shape functions N_i, where the nodal unknowns $e_i^{(n)}$ and $h_i^{(n)}$ represent the values of $\tilde{E}_{sy}$ *and* $\tilde{H}_{sy}$ at four corner and four mid-side nodes:

$$\hat{E}_{sy}^{(n)}=\sum_{i=1}^{8}N_i e_i^{(n)} \quad \text{and} \quad \hat{H}_{sy}^{(n)}=\sum_{i=1}^{8}N_i h_i^{(n)}. \tag{3}$$

For each element, the coupled field equations can be expressed in matrix form:

$$K^{(n)}f^{(n)}=\text{-}S^{(n)} \tag{4}$$

where $K^{(n)}$ is the 16×16 symmetric, banded stiffness matrix, $f^{(n)}$ is the 16-component vector of nodal unknowns (eight electric and eight magnetic field values), and $S^{(n)}$ is the effective source vector. These element matrices are assembled into a global system, with boundary conditions incorporated into $S^{(n)}$.

Dirichlet boundary conditions are applied by matching the boundary fields to a one-dimensional earth model along each domain edge. In cases where lateral conductivity contrasts exist, boundary nodes are placed sufficiently far from the region of interest to avoid numerical instability. The flexibility of the isoparametric formulation allows for variable node spacing in both lateral and vertical directions, which reduces computational cost without sacrificing accuracy.

The assembled global system is solved using a direct frontal solution method, which is a row-by-row scheme that minimizes memory requirements and reduces arithmetic operations compared to standard LU decomposition. This method is particularly advantageous for quadratic basis functions, as these functions typically increase matrix bandwidth.

Following the solution of the coupled field equations for $\tilde{E}_{sy}$ *and* $\tilde{H}_{sy}$ across the discretized k_y spectrum, the next step involves constructing the frequency-domain secondary magnetic field response, $H_s(x,y,z,\omega)$. The modeling process spans a frequency range from 1 Hz to 100 kHz, sampled logarithmically at six points per decade. Each frequency-domain problem is

decomposed into 21 subproblems in the k_y domain, with k_y values ranging from 10^{-5} to 1, sampled logarithmically at five points per decade. This decomposition allows the distributed three-dimensional source to be represented efficiently as a direct computation in the k_y domain, ensuring that the resulting field contributions are accurately reconstructed.

For each k_y value, the previously described isoparametric finite-element approach, combined with the frontal solution method, is used to obtain $\tilde{E}_{sy}$ *and* $\tilde{H}_{sy}$. The cross-strike and vertical magnetic field components, $\hat{H}_{sx}$ *and* $\hat{H}_{sz}$, are then computed from the following relations:

$$\hat{H}_{sz} = -\alpha \left[ik_y \left(\hat{J}_{Dx} + \frac{\partial \hat{H}_{sy}}{\partial z} \right) + \sigma \frac{\partial \hat{E}_{sy}}{\partial x} \right] \tag{5}$$

And

$$\hat{H}_{sx} = \alpha \left[ik_y \left(\hat{J}_{Dz} - \frac{\partial \hat{H}_{sy}}{\partial x} \right) + \sigma \frac{\partial \hat{E}_{sy}}{\partial z} \right] \tag{6}$$

where $\alpha = (k_y^2 + i\omega\mu\sigma(x,y))^{-1}$.

The results for $\hat{H}_{sx}$, $\hat{H}_{sz}$, and $\hat{H}_{sy}$ are combined across the k_y domain using cubic spline interpolation. This continuous representation of the field components enables the computation of $H_s(x,y,z,\omega)$ by applying a digital filter to the spline-fitted solutions, ensuring smooth frequency-domain responses over the full bandwidth.

After constructing the frequency-domain secondary magnetic field $H_s(x,y,z,\omega)$ using cubic spline interpolation of $\hat{H}_s(x,k_y,z,\omega)$, a digital filter is applied to produce a smooth and continuous representation suitable for time-domain transformation. The secondary step-response magnetic field, $h_s(x,y,z,t)$, can be derived by applying a cosine transform of the imaginary part of $H_s(x,y,z,\omega)/\omega$. This operation converts the frequency-domain solution into the time domain while preserving the phase and amplitude characteristics of the response.

The complete system response is then calculated by convolving the sum of the analytically derived step-response field for the normal reference medium, $h_n(x,y,z,t)$, and the computed secondary response, $h_s(x,y,z,t)$, with the time derivative of the transmitter waveform. The resulting signal is scaled by the magnetic permeability to yield the physical magnetic field variation. Finally, the observed TDEM response, expressed as db/dt, is determined by differencing the convolved signal across the receiver time windows, producing the measurable decay curves used for interpretation.

Constrained Occam and Conjugate Gradient Method

In regularized electromagnetic (EM) inversion, as described by Parker (1994) and Zhdanov (2002), the solution is obtained by minimizing a functional that combines model smoothness, deviation from a reference model, and data misfit (Parker, 1994; Zhdanov, 2015). The functional is defined as:

$$U = \| Rm \|^2 + \| P(m - m_*) \|^2 + \mu^{-1} \| W(d - \mathrm{F}\ (m)) \|^2 \tag{7}$$

In this expression, m is an *n*-dimensional parameter vector expressed in $\log_{10}(resistivity)$. The first component controls the roughness of the solution, the second ensures proximity to the prior model m_*, and the last term accounts for the agreement between the predicted response F (m) and the measured data d, scaled by the inverse data uncertainties using the diagonal weighting matrix W. The prejudice component can be excluded in most cases, with its diagonal weighting matrix P generally assigned as zero. When a specific group of model parameters needs to be emphasized, the diagonal elements of P may be set to positive values, allowing the preferred resistivity to be incorporated into m_*. The Lagrange multiplier μ adjusts the balance between fitting the data and controlling model smoothness and prior bias, which helps stabilize the inverse solution, particularly when the problem is ill-conditioned.

The Occam method, introduced by Constable et al. (1987), represents a modified form of nonlinear Gauss–Newton minimization that is commonly applied in geophysical studies (Constable et al., 1987). This method simplifies the functional by linearizing it around an initial model $\mathbf{m}_k$ and performs the minimization through iterative updates.

$$m_{k+1} = \left[\mu \left(R^T R + P^T P \right) + \left(W J_k \right)^T W J_k \right]^{-1} \times \left[\left(W J_k \right)^T W \hat{d} + \mu P^T P m_* \right] \tag{8}$$

where the modified data vector

$$\hat{d} = d - \mathrm{F}\,(m_k) + J_k m_k \tag{9}$$

The Jacobian matrix J contains elements:

$$J_{ij} = \frac{\partial \mathrm{F}_i(m_k)}{\partial m_j} = \frac{\partial \mathrm{F}_i(m_k)}{\partial \log_{10} \rho_j} = -\frac{\ln(10)}{\rho_j} \frac{\partial \mathrm{F}_i(m_k)}{\partial \sigma_j} \tag{10}$$

The sensitivities $\partial \mathrm{F}_i(m_k) / \partial \sigma_j$ are computed efficiently using the procedure described earlier. Phase 1 of the Occam algorithm involves a line search over μ in equation (8) to determine the value that generates m_{k+1} with the lowest data misfit, even if the initial misfit exceeds the target threshold. In the original implementation, this process brackets the minimum using a golden-section search, followed by refinement with Brent's method (Press et al., 2003). Each iteration begins with the evaluation of the Jacobian $J(m_k)$ along with a forward computation F (m_k) to assess the misfit of the current model, after which the line search is executed. When the minimum is quickly bracketed and located, four forward model evaluations are sufficient. However, some iterations may require up to six forward calls, and in certain cases, as many as nine or ten iterations are needed during an Occam update. This adaptive search over μ enables the method to locate models with improved fit, though the number of forward computations can become computationally demanding. Consequently, many alternative algorithms adopt a fixed μ value, adjusting it only when no satisfactory model can be obtained (see (Press et al., 2003; Siripunvaraporn, 2012)).

During initial iterations, the minimum search often produces model misfits that remain higher than the target threshold, even when local minima are reached. In the standard Occam procedure, the search continues until a sufficient reduction in misfit is obtained, with a root-mean-squared (rms) misfit reduction threshold of about 15% typically considered effective for most EM inversion cases. This threshold ensures the search continues until at least a 15% reduction in rms misfit is achieved; if the reduction is less, a smaller model adjustment is applied by halving the step size, and the line search is repeated using the updated model m'_{k+1}:

$$m'_{k+1} = \alpha m_{k+1} + (1 - \alpha) m_k \tag{11}$$

The initial step size is set to $\alpha = 1$, and it is halved iteratively whenever the line search fails to obtain a model with an improved fit.

Once a model achieves a misfit equal to or below the target threshold, phase 2 of the Occam algorithm begins. At this stage, the procedure identifies the model corresponding to the target misfit with the largest μ, which results in the smallest roughness norm, or smoothest model. This is achieved by bracketing μ around the target misfit and applying interpolation to determine the maximum value of μ at the target misfit.

The model update described in equation (8) does not explicitly constrain the range of permissible parameter values. However, in many cases, geological information or supporting datasets suggest that conductivity should remain within a specific range. To incorporate such bounds, the inverse problem may be reformulated using a non-linear transformation of the model parameters, ensuring consistency with the unconstrained formulation (Box, 1966). In this approach, the model parameter *m* is constrained as:

$$I < m(x) < u \tag{12}$$

while the transformed parameter *x* remains unbounded:

$$-\infty < x(m) < \infty \tag{13}$$

Using the transformed model vector x, the model update is expressed through a modified form of equation (8):

$$x_{k+1} = \left[\mu \left(R^T R \right) + \left(W J_k^* \right)^T W J_k^* \right]^{-1} \left[\left(W J_k^* \right)^T W \hat{d} \right] \tag{14}$$

Where:

$$\hat{d} = d - \mathrm{F}\ (m_k) + J_k^* x_k \tag{15}$$

$$J_{ij}^* = \frac{\partial m_j}{\partial x_j} J_{ij} \tag{16}$$

A major computational challenge in Occam inversion arises from handling the dense matrices in the updated formulation of equation (8) when the model size is large. For n model parameters, storing $(WJ)^T WJ$ requires n^2 values in memory. Additionally, matrix-matrix multiplications and factorization steps for solving the linear system involve computational costs that scale as $O(n^3)$. For large-scale problems, these operations can consume far more time than calculating the forward response and assembling the Jacobian. To reduce this computational burden, the inversion uses the conjugate gradient method, which avoids explicit storage of J by relying solely on matrix-vector products involving J or its transpose. These products are computed as needed, significantly reducing memory requirements while maintaining efficiency. The CG method operates iteratively, reducing memory usage from $O(n^2)$ to $O(n)$ by storing only vectors, unlike direct factorization.

Case study

The Bell polymetallic deposit, located on the Newman Peninsula at the northern end of Babine Lake in British Columbia, Canada, is a key porphyry system in the Babine Lake region. It was formed by the intrusion of Eocene biotite-feldspar porphyry (BFP) and biotite-quartz-feldspar porphyry (BQFP) stocks into Early Cretaceous argillaceous sediments and rhyolite domes of the Skeena Group (Figure 1).

The deposit's position is controlled by the intersection of the northwest-trending Newman Fault and an east-northeast fault, within graben structures developed during Late Cretaceous to Early Tertiary extension (Dirom et al., 1995). Hydrothermal alteration at Bell features a central potassic zone with biotite, quartz, and magnetite, surrounded by propylitic alteration and overprinted by phyllic (quartz-sericite-pyrite) zones. Mineralization occurs as sulfides, with higher grades linked to phyllic alteration and a broad pyrite halo over 1100 m (Mitchinson, 2013). This alteration pattern makes Airborne TDEM surveys ideal for this site due to their sensitivity to conductive sulfide bodies in rugged, complex terrain.

An airborne time-domain electromagnetic (TDEM) survey was conducted in October 2008 over the Bell deposit using the AeroTEM III system. As shown in Figure 2, the survey consisted of 21 east-west flight lines spaced 200 m apart, with one perpendicular tie line included for quality control. The electromagnetic sensor operated at a nominal terrain clearance of 30 m, with adjustments in rugged areas for safety. Data were sampled at 10 Hz, providing readings every 1.5–2.5 m along the flight path. The system utilized a triangular waveform with a symmetric on-time pulse of 1.71 ms and a base frequency of 90 Hz, alternating polarity each cycle. As shown in Figure 3, raw data captured 200 channels per cycle at 27.78 μs width, which were processed post-survey into 33 stacked on- and off-time channels for the X and Z components (Walker, 2009). The central segment of line 1110, which passes over the Bell mine pit, was selected for inversion as it traverses the primary deposit zone and detects key conductive anomalies.

The observed dB/dt data, shown in Figure 4, cover 17 off-time channels and include the modeled section's position, revealing responses from subsurface conductors.

The inversion was carried out using ArjunGUI software, which implements 2.5D modeling and constrained Occam inversion with conjugate gradient (CG) optimization for airborne TDEM data. For this inversion, off-time channels were prioritized due to their lower noise levels, making them more effective for resolving certain subsurface conductivities (Balch et al., 2003). The setup involved generating an initial resistivity model based on the observed data profile, with a background resistivity of 8000 Ωm and a mesh discretization of 137 × 20 nodes, incorporating topography and a nominal cell size of 25 m horizontally and 10 m vertically at the surface.

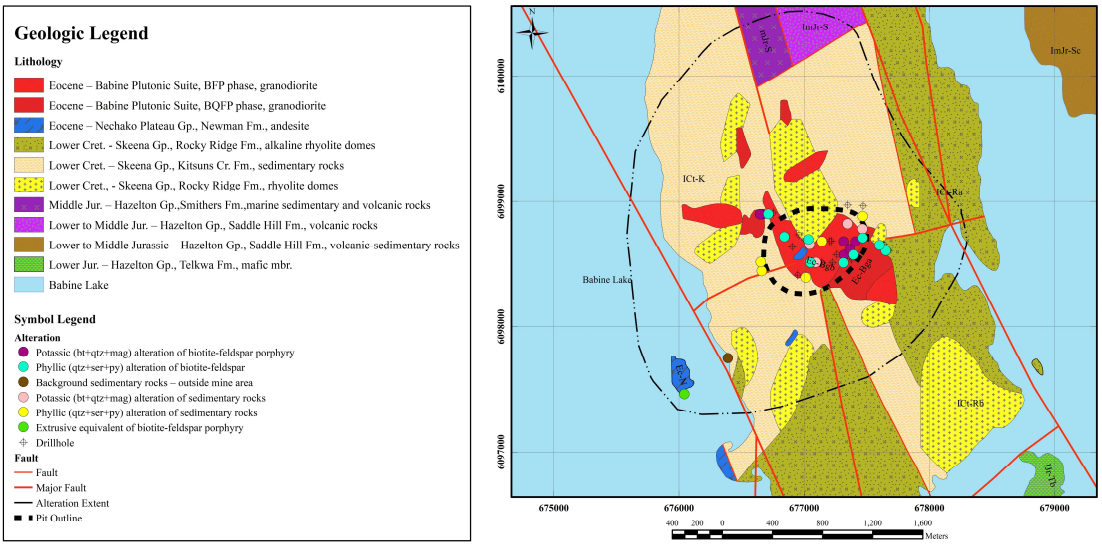

Figure 1. Geological map of the studied area, Bell polymetallic deposit in BC, Canada

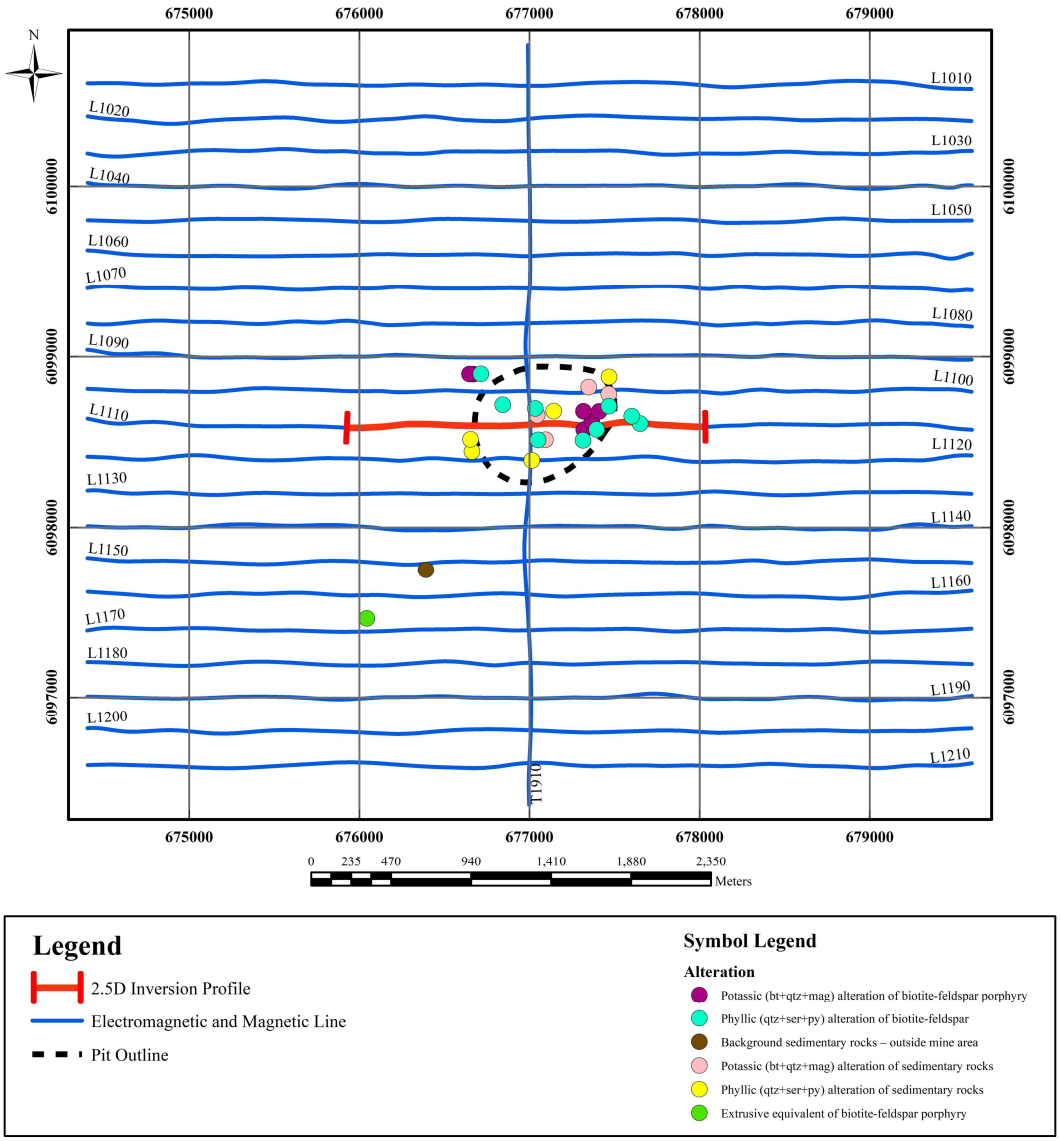

Figure 2. Airborne TDEM survey layout over the area, and the studied line 1110

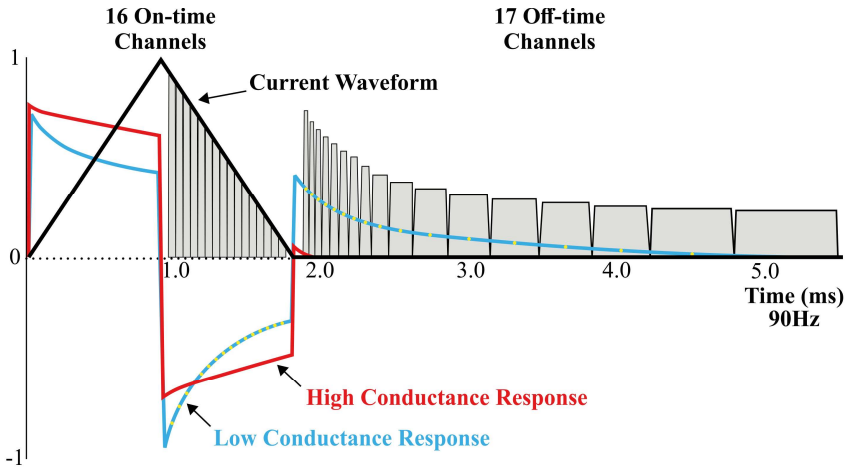

Figure 3. Schematic representation of curves for current wave form in the EM transmitter and inductive response obtained in the receiver (Walker, 2009)

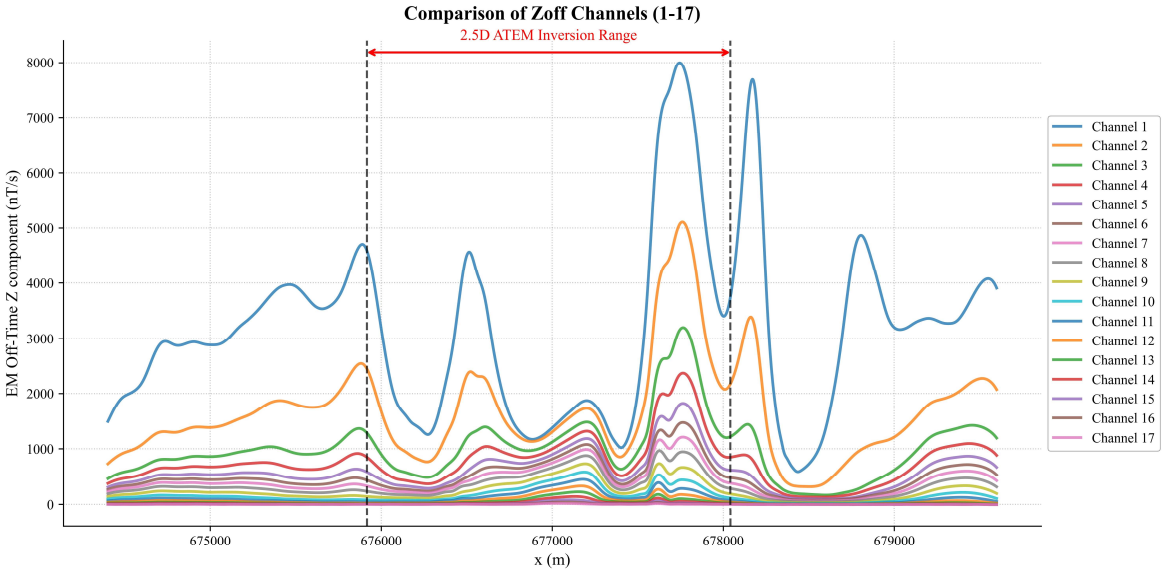

Figure 4. Observed dB/dt data along line L1110, and the modeled data position

Mesh density was increased in the central section, where conductive structures were more likely, by halving horizontal cell sizes. Constraints were applied by fixing cells in the margins and deeper layers to reflect geological priors, while free cells allowed variation. Key parameters included a Lagrange multiplier of 1 for balancing misfit and smoothness, a noise threshold of 0.01 nT/s to exclude unreliable data points, and a maximum log-step of 1.5 to stabilize iterations. Inversion proceeded through iterative adjustments, minimizing data misfit and model roughness via CG solutions. Resistivity values were updated until convergence at a target RMS of 10% after 29 iterations, producing smooth, geologically consistent distributions.

The inversion achieved a close fit between observed and predicted dB/dt data across the off-time channels along line 1110. Figure 5 illustrates this for the first nine channels, where predicted responses align well with observed dB/dt data, validating the model's reliability. The outputs include a resistivity model (Figure 6), which reveals zones of varying resistivity associated with hydrothermal alterations. The resistivity model displays prominent low-resistivity anomalies centered at approximately 100 m depth in the model's central area, with scattered patches of low resistivity at shallow depths observed around them. These shallow patches correlate with sampled phyllic alteration zones featuring quartz-sericite-pyrite overprinting biotite-feldspar porphyry, indicating conductive features tied to hydrothermal processes. The anomalies separate along a central line that aligns with inferred fault extensions from surface geological maps (Mitchinson, 2013), suggesting fault-related fracturing enhanced fluid flow and alteration.

High-resistivity areas delineate potassic alteration zones effectively, where elevated susceptibility was inferred from prior geophysical data, providing clear zoning for exploration targeting. This comparison with available geological and geophysical data validates the recovered resistivity model. Surface alteration samples further confirm shallow low-resistivity patches, and the model is consistent with prior geophysical studies showing high magnetic susceptibility zones (Figure 7a) in mid-depths, indicating potassic alteration with secondary biotite and magnetite, and a deeper positive density contrast (Figure 7b) which suggests a magmatic intrusion structure (Jafarabadi, 2025). Based on these geophysical models and geological information, which corroborates the phyllic and potassic alteration patterns (Dirom et al., 1995), a conceptual alteration model has been created, as shown in Figure 8.

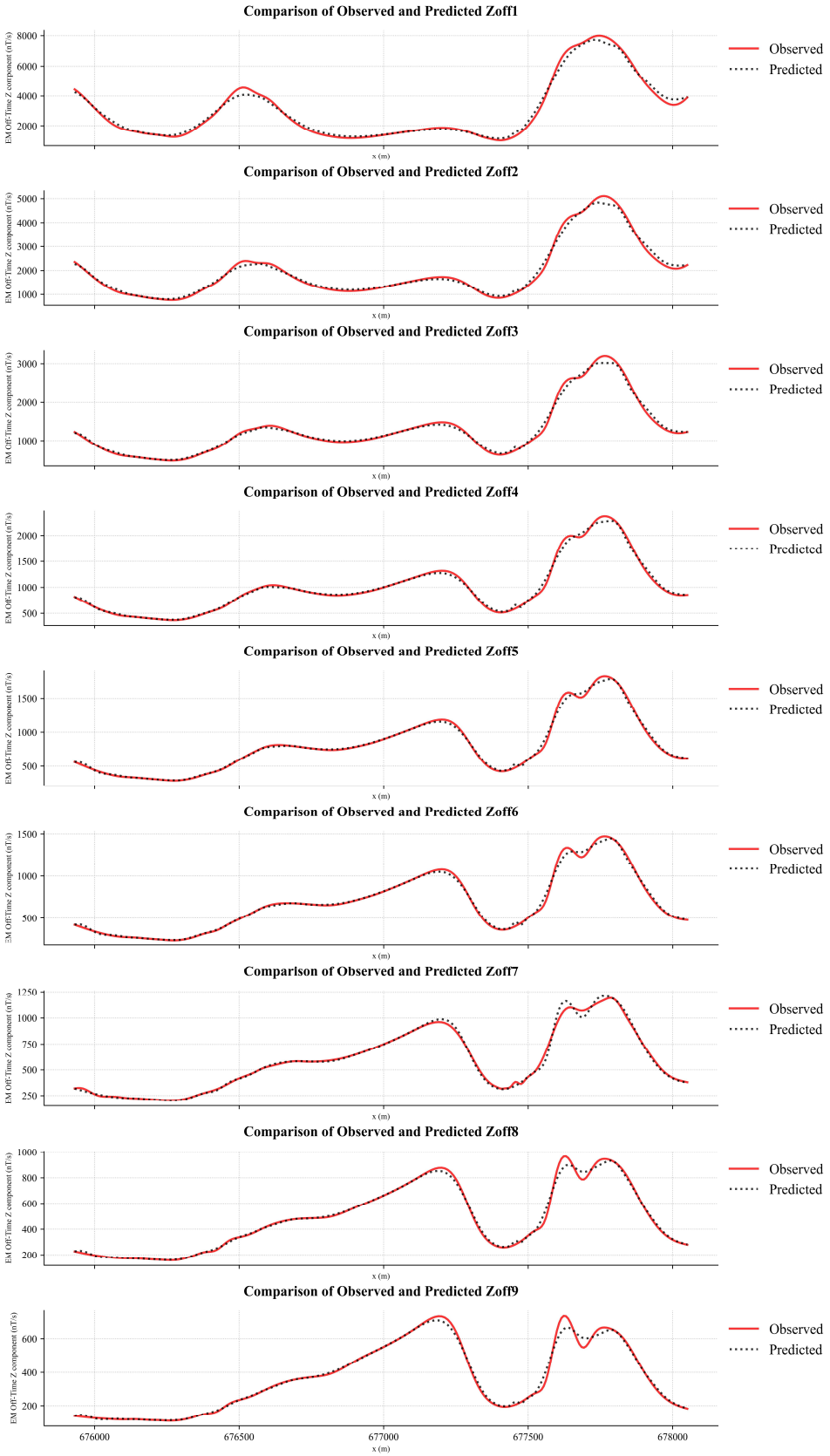

Figure 5. Observed and predicted electromagnetic db/dt data in nine off-time channels along line L1110

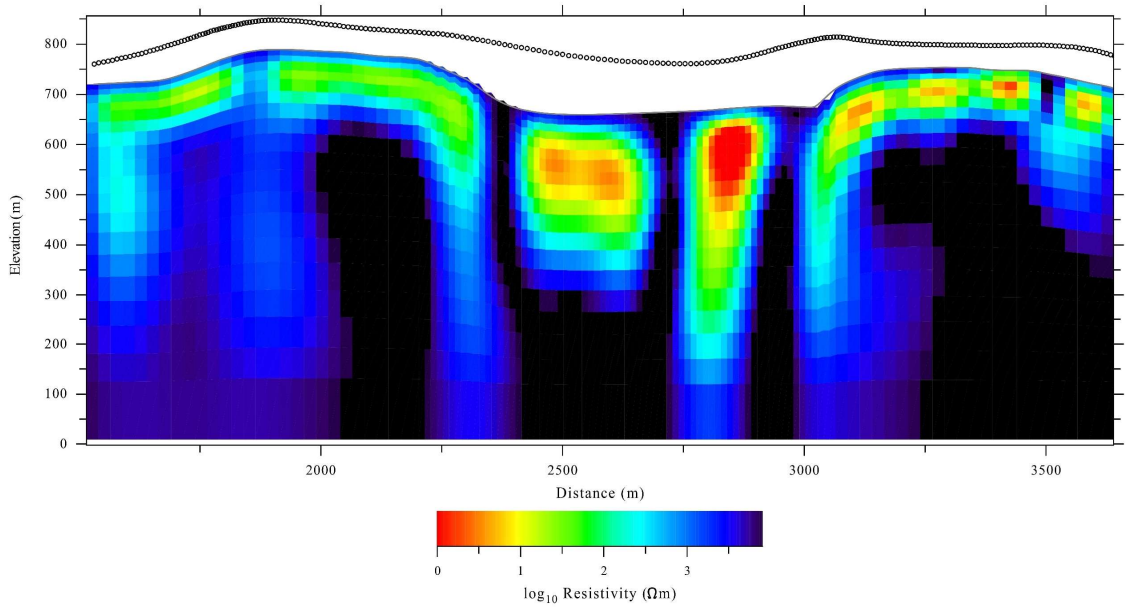

Figure 6. 2.5D resistivity model derived from inversion of airborne TDEM data along line L1110

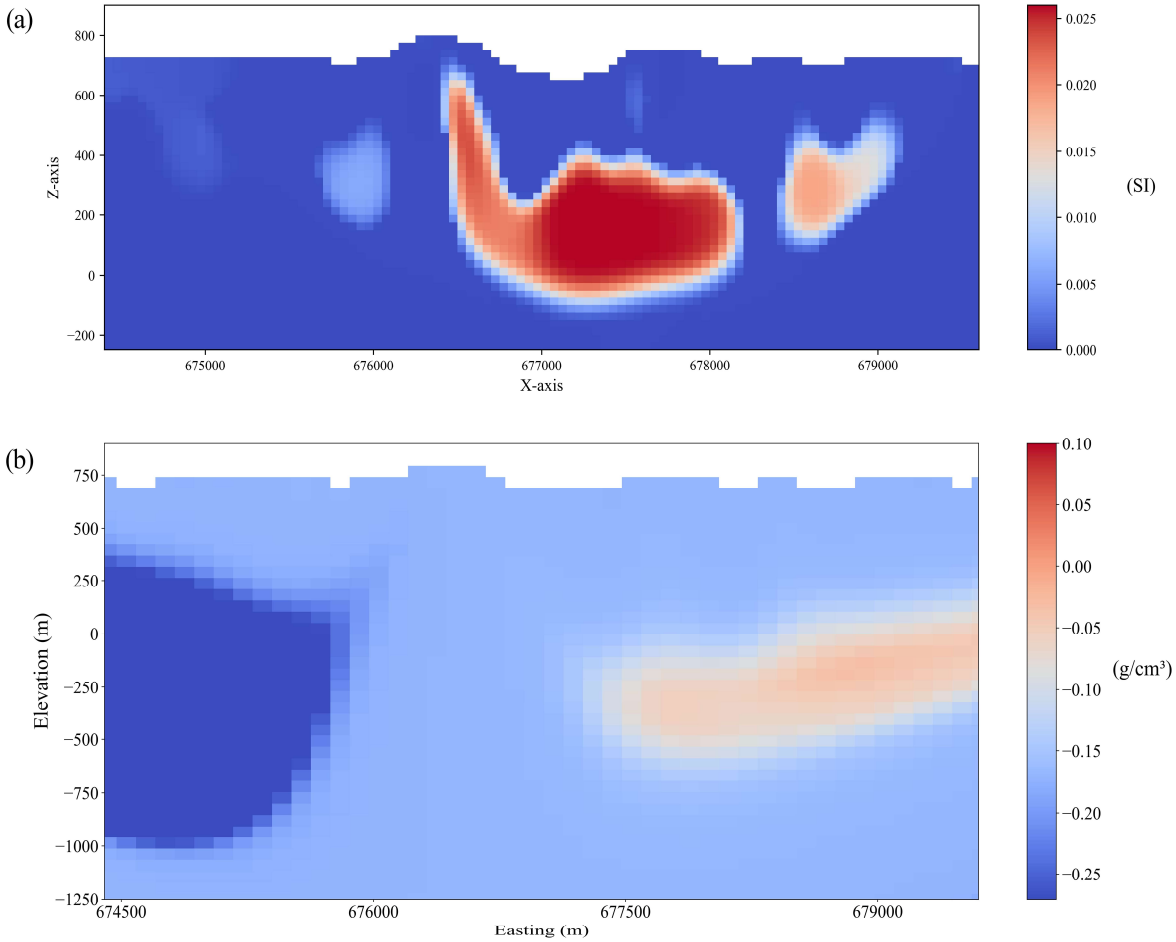

Figure 7. Magnetic susceptibility model (a) and density contrast model (b) along line L1110 (Jafarabadi, 2025)

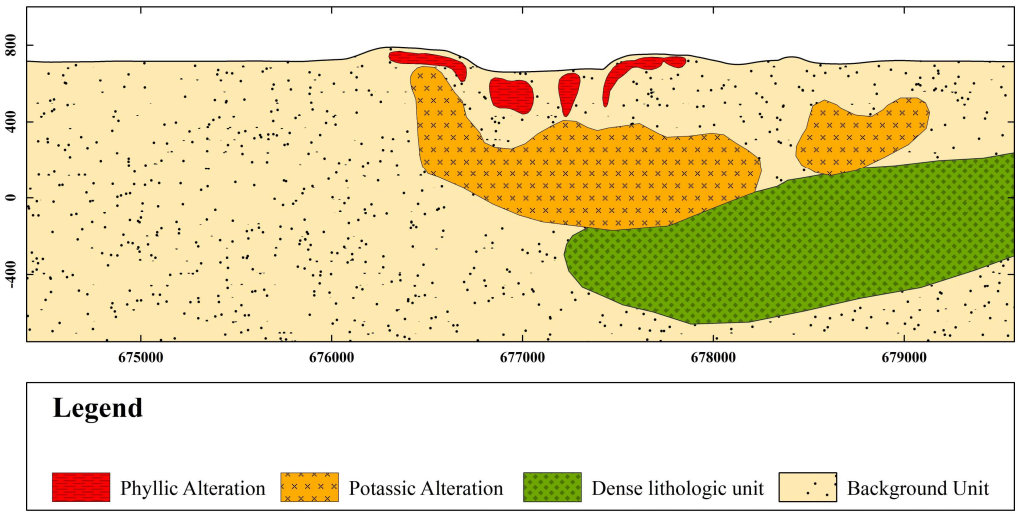

Figure 8. Plausible alteration model derived from this research and previous studies

Conclusion

This study applied 2.5D inversion to airborne TDEM data through the constrained Occam and conjugate gradient method. This method effectively imaged the subsurface structure of the Bell polymetallic deposit. Key findings include low-resistivity zones at approximately 100 m depth, linked to phyllic alteration. These zones also indicate potential fault structures that could enhance fluid flow and mineralization. The resistivity model matches well with prior geological and geophysical data, including the locations of known alteration zones and high-susceptibility areas related to potassic alteration. Overall, the method managed the complex terrain successfully, yielding smooth and geologically consistent models. This approach provides broader value in mineral exploration by improving the detection of conductive zones associated with phyllic alteration, which aids targeted drilling and resource assessment in porphyry systems. It provides advantages over 1D methods in terms of better accuracy and over 3D methods in terms of lower computational costs. While this study demonstrates the effectiveness of 2.5D TDEM inversion for porphyry deposits like the Bell deposit, the method's ability to resolve conductive anomalies makes it applicable to other polymetallic deposits, such as volcanogenic massive sulfide (VMS) or skarn deposits, which similarly feature conductive sulfide mineralization. However, successful application to these deposits may require adjustments in survey parameters, such as flight line spacing or time-channel selection, to account for variations in deposit size, depth, or host rock properties. These adaptations ensure the method's versatility across diverse geological settings, although limitations, such as noise in late-time channels, may still affect the results. Unlike conventional 1D methods, which cannot resolve complex geological systems or distinguish their features, offering only a broad overview of the geology, this 2.5D inversion effectively delineates alteration zones, fault structures, and related geological features. The resistivity models enhance understanding of hydrothermal alteration zones tied to the deposit's polymetallic potential.

Despite these strengths, limitations include high noise levels in late-time TDEM channels, which leads to the exclusion of substantial data points based on the defined noise threshold and thus restricting usable information for inversion. Another constraint concerns mesh discretization in the software, where inappropriate cell sizing may affect modeled shapes and cause layers to distort under topographic effects. Future work should address these issues by refining mesh discretization techniques to minimize such distortions, ensuring more accurate representations in rugged terrains.

Acknowledgements

The authors wish to express their heartfelt gratitude to the School of Mining Engineering at the University of Tehran for their invaluable support. Additionally, we extend our sincere appreciation to Geoscience BC in Canada for generously providing the essential data that contributed to this work.

Authors' contributions

Ali Jafarabadi: Writing Original Draft, Algorithm and Software Execution. Maysam Abedi: Editing Manuscript, Methodology Proposing and Supervisor. Ali Moradzadeh: Supervisor and Checking the Results.

Conflicts of interest

The authors have no competing interests to declare that are relevant to the content of this article.

References

Abubakar, A., Habashy, T., Druskin, V., Knizhnerman, L., Alumbaugh, D., 2008. 2.5D forward and inverse modeling for interpreting low-frequency electromagnetic measurements. Geophysics 73: F165-F177.

Auken, E., Boesen, T., Christiansen, A.V., 2017. A review of airborne electromagnetic methods with focus on geotechnical and hydrological applications from 2007 to 2017. In: Nielsen, L. (Ed.), Advances in Geophysics, 58: 47-93.

Balch, S.J., Boyko, W.P., Paterson, N.R., 2003. The AeroTEM airborne electromagnetic system. The Leading Edge 22: 562-566.

Box, M., 1966. A comparison of several current optimization methods, and the use of transformations in constrained problems. The Computer Journal 9: 67-77.

Chang-Chun, Y., Xiu-Yan, R., Yun-He, L., Yan-Fu, Q., Chang-Kai, Q., Jing, C., 2015. Review on airborne electromagnetic inverse theory and applications. Geophysics 80: W17-W31.

Constable, S.C., Parker, R.L., Constable, C.G., 1987. Occam's inversion: A practical algorithm for generating smooth models from electromagnetic sounding data. Geophysics 52: 289-300.

Dirom, G.E., Dittrick, M.P., McArthur, D.R., Ogryzlo, P.L., Pardoe, A.J., Stothart, P.G., 1995. Bell and Granisle porphyry copper-gold mines, Babine region, west-central British Columbia. In: Schroeter, T.G. (Ed.), Porphyry Deposits of the Northwestern Cordillera of North America, Vol. 46. Canadian Institute of Mining, Metallurgy and Petroleum, pp. 256-289.

Ellis, R.G., 1998. Inversion of airborne electromagnetic data. Exploration Geophysics 29: 121-127.

Engebretsen, K.W., Zhang, B., Fiandaca, G., Madsen, L.M., Auken, E., Christiansen, A.V., 2022. Accelerated 2.5D inversion of airborne transient electromagnetic data using reduced 3D meshing. Geophysical Journal International 230: 643-653.

Everett, M.E., Edwards, R.N., 1993. Transient marine electromagnetics: The 2.5D forward problem. Geophysical Journal International 113: 545-561.

Guo, Z., Xue, G., Liu, J., Wu, X., 2020. Electromagnetic methods for mineral exploration in China: A review. Ore Geology Reviews 118: 103357.

Jafarabadi, A., 2025. Geophysical modeling of airborne time-domain electromagnetic and potential field data in the Bell polymetallic deposit: British Columbia, Canada. M.Eng. thesis, University of Tehran, College of Engineering, School of Mining Engineering.

Ke, Z., Liu, L., Huang, L., Zhao, Z., Ji, Y., Liu, X., Fang, G., 2023. An efficient 2.5D forward algorithm based on the spectral element method for airborne transient electromagnetics data. Geophysical Prospecting 71: 1056-1069.

Li, W.-B., Zeng, Z.-F., Li, J., Chen, X., Wang, K., Xia, Z., 2016. 2.5D forward modeling and inversion of frequency-domain airborne electromagnetic data. Applied Geophysics 13: 37-47.

McMillan, M.S., Schwarzbach, C., Oldenburg, D.W., Haber, E., Holtham, E., Prikhodko, A., 2014. Recovering a thin dipping conductor with 3D electromagnetic inversion over the Caber deposit. SEG

Technical Program Expanded Abstracts, SEG, pp. 180-184
Mitchinson, D.E.E., Enkin, R.J., Hart, C.J.R., 2013. Linking porphyry deposit geology to geophysics via physical properties: Adding value to Geoscience BC geophysical data. Geoscience BC Report, 116 pp.
Núñez, P., Watts, T., Martin-Izard, A., Arias, D., Rubio, Á., Cortés, F., Díaz-Riopa, F., 2023. Airborne electromagnetic survey over the Touro copper VMS world-class deposit (NW Spain): Geological and geophysical correlation. Minerals 13: 17.
Oldenburg, D., 1999. Applications of geophysical inversions in mineral exploration. SEG Technical Program Expanded Abstracts, Society of Explorayion Geophysicists.
Oldenburg, D., Pratt, D.A., 2007. Geophysical inversion for mineral exploration: A decade of progress in theory and practice. Proceedings of Exploration 07: Fifth Decennial International Conference on Mineral Exploration, pp. 61-95.
Oldenburg, D.W., Li, Y., Ellis, R.G., 1997. Inversion of geophysical data over a copper-gold porphyry deposit: A case history for Mt. Milligan. Geophysics 62: 1419-1431.
Palacky, G.J., West, G.F., 1991. Airborne electromagnetic methods. In: Nabighian, M.N. (Ed.), Electromagnetic Methods in Applied Geophysics: Application, Parts A and B. Society of Exploration Geophysicists, 2: 811-880.
Parker, R.L., 1994. Geophysical inverse theory, Vol. 1. Princeton University Press, 400 pp.
Paterson, R., Silic, J., FitzGerald, D., 2016. Improved structural mapping and conductive targeting delivered by a new 2.5D AEM inversion solver. ASEG Extended Abstracts, 2016: 1-8.
Pirttijärvi, M., 2014. ArjunGUI—2.5D modelling and inversion of time-domain EM data: User's guide to version 1.0.
Press, W.H., Teukolsky, S.A., Vetterling, W.T., Flannery, B.P., 2003. Numerical recipes in Fortran 77, Cambridge University Press, 1: 1010 pp.
Raiche, A., Annetts, D., Sugeng, F., 2001. EM target response in complex hosts. ASEG Extended Abstracts, 2001: 1-4.
Raiche, A., Sugeng, F., Annetts, D., 2003. Finding targets in complex hosts using airborne EM. ASEG Extended Abstracts, 2003: 1-4.
Shah, A.K., Bedrosian, P.A., Anderson, E.D., Kelley, K.D., Lang, J., 2013. Integrated geophysical imaging of a concealed mineral deposit: A case study of the world-class Pebble porphyry deposit in southwestern Alaska. Geophysics 78: B317-B328.
Silic, J., Paterson, R., FitzGerald, D., Archer, T., 2015. Comparing 1D and 2.5D AEM inversions in 3D geological mapping using a new adaptive inversion solver. In: 14th International Congress of the Brazilian Geophysical Society & EXPOGEF, Rio de Janeiro, Brazil, 3-6 August 2015, pp. 184-189.
Sinclair, W.D., 2007. Porphyry deposits. In: Goodfellow, W.D. (Ed.), Mineral Deposits of Canada - A Synthesis of Major Deposit Types, District Metallogeny, the Evolution of Geological Provinces, and Exploration Methods, Special Publication 5. Geological Association of Canada, Mineral Deposits Division, pp. 223-243.
Siripunvaraporn, W., 2012. Three-dimensional magnetotelluric inversion: An introductory guide for developers and users. Surveys in Geophysics 33: 5-27.
Smith, R., 2014. Electromagnetic induction methods in mining geophysics from 2008 to 2012. Surveys in Geophysics 35: 123-156.
Sugeng, F., Raiche, A., Rijo, L., 1993. Comparing the time-domain EM response of 2-D and elongated 3-D conductors excited by a rectangular loop source. Journal of Geomagnetism and Geoelectricity 45: 873-885.
Unsworth, M., Travis, B., Chave, A., 1993. Electromagnetic induction by a finite electric dipole source over a 2-D Earth. Geophysics 58: 198-214.
Walker, S.G., Doug, 2009. Report on a helicopter-borne AeroTEM system electromagnetic & magnetic survey (QUEST West Project).
Wilson, G., Raiche, A., Sugeng, F., 2006. 2.5D inversion of airborne electromagnetic data. Exploration Geophysics 37: 363-371.
Yu, W.W., Haber, E., 2012. A 2.5D inversion of airborne electromagnetic data. SEG International Exposition and Annual Meeting, Expanded Abstracts.
Zhdanov, M.S., 2015. Inverse theory and applications in geophysics, 36: 730.

This article is an open-access article distributed under the terms and conditions of the Creative Commons Attribution (CC-BY) license.